This is the Pre-Published Version.

The following publication X. Xiong, C. K. Tse and X. Ruan, "Bifurcation Analysis and Experimental Study of a Multi-Operating-Mode Photovoltaic-Battery Hybrid Power System," in IEEE Journal on Emerging and Selected Topics in Circuits and Systems, vol. 5, no. 3, pp. 316-325, Sept. 2015 is available at https://doi.org/10.1109/JETCAS.2015.2462015.

Bifurcation Analysis and Experimental Study of a Multi-Operating-Mode Photovoltaic-Battery Hybrid Power System

Xiaoling Xiong, Chi K. Tse, *Fellow, IEEE,* and Xinbo Ruan, *Senior Member, IEEE*

***Abstract*—The stand-alone hybrid renewable power generation systems for local applications have gained popularity in recent years. However, due to the intermittent nature of the renewable resources, the hybrid renewable power generation systems are often designed to operate with multiple structures and multiple operating modes. The design for stable operation of such systems requires consideration of the stability conditions for all possible structures and operating modes. As a system of practical importance, the stand-alone photovoltaic-battery hybrid power system is studied for illustrating the possible complex behavior in this paper. We reveal smooth bifurcation in this system, including slow-scale Neimark-Sacker bifurcation, fast-scale period-doubling bifurcation as well as coexisting bifurcation. Under certain conditions, when the system switches its operating mode, a non-smooth bifurcation, manifested as a jump between stable and unstable behavior, can also be observed. Moreover, a detailed analysis based on a discrete-time mapping model is performed to identify these bifurcation phenomena and evaluate the stability boundaries of the system. Extensive experiments verify the theoretical analysis and simulated results.**

***Index Terms*—Bifurcation, fast-scale instability, low-scale instability, photovoltaic-battery hybrid system.**

I. Introduction

GLOBAL environmental concerns and increased demand for energy consumption, coupled with a steady development of renewable energy technologies, are opening up new opportunities for developing renewable power generation systems [1]. For localized applications in some remote non-electrified regions, constructing stand-alone power generation systems is often more cost-effective than the conventional deployment of the grid-connected power generation system [2]–[9]. However, as climate, solar radiation, wind speed, etc. vary from time to time, the availability of energy from renewable sources is not always predictable. Thus, a power system that depends entirely upon multiple renewable energy sources can be unreliable. In order to provide continuous electrical power to the load, the use of energy storages in stand-alone renewable power generation systems is usually adopted. The renewable energy sources and energy storages can be connected to a common dc bus via a number of power converters [4]–[10]. In some applications, the power sources are close to the load, and multiple-input converters [11] or multiple-port bidirectional converters [2], [12] can be used as interface conversion systems. Regardless of the exact topologies used, the switching circuits and control systems are required to regulate the dc bus voltage and maximize the use of renewable energy, as well as balance the power from all sources. Then, the renewable power conversion unit may operate in a maximum power point tracking (MPPT) mode or off-MPPT mode, and at the same time, the energy storage unit may provide power to the load or store energy from the renewable power sources. The whole system is thus designed to operate with multiple structures and multiple operating modes [3], [5]–[12]. As a result, the dynamics of such a system is rather complex. The closed-loop design has to take into consideration the different modes of operation. It can thus be appreciated that the stability issue is non-trivial as the system assumes different structures in different operating modes under different ranges of parameters.

For most power electronics systems, normal stable operation refers to stable period-1 operation, which is often the expected operating regime for practical applications. Operation states that are not the normal operation are practically regarded as unstable states, and the bifurcation refers to the change from one type of operation to another. As of now, a rich set of nonlinear phenomena have been investigated in power electronic circuits, such as period-doubling bifurcation [13]–[18], Neimark-Sacker bifurcation [19], saddle-node bifurcation [20], border collision [20]–[22] and chaos [14]–[21]. Due to the change of switching structure, border collision as a type of non-smooth bifurcation has been found in many switching systems, which is characterized by a discontinuous 'jump' in the eigenvalues of the Jacobian as some parameters are varied continuously [21]. In such a case, the duty cycle becomes saturated as it is bounded between 0 or 1. In recent years, the nonlinear stability analysis has been extended to more complex conversion systems, such as the high order Ćuk converter [23], [24], single-inductor dual-switching dc-dc converters [25], multichannel converters [26], [27], and grid-connected power converters [28]–[30]. However, the dynamics of a multi-structure multi-operating-mode system has rarely been formally discussed in the literature [31], [32]. To illustrate the possible complex behavior in this kind of system, a commonly used multi-operating-mode stand-alone photovoltaic-battery hybrid power system (PBHPS) is studied in this paper, which is based on a solar power system and a

Manuscript received March 1, 2015; revised September 2, 2019. This work is supported by Hong Kong Research Grants Council GRF Project PolyU 5258/13E.

X. Xiong and X. Ruan are with the College of Automation Engineering, Nanjing University of Aeronautics and Astronautics, Nanjing, China. (Email: xiong_xl1102@nuaa.edu.cn; ruanxb@nuaa.edu.cn)

C.K. Tse is with the Department of Electronic and Information Engineering, Hong Kong Polytechnic University, Kowloon, Hong Kong, China. (Email: encktse@polyu.edu.hk)

Digital Object Identifier 00.0000/JETCAS.2015.0000000000

battery connected to an output dc bus via a boost converter and a bidirectional buck-boost converter, respectively.

II. Photovoltaic-Battery Hybrid Power System

A. PBHPS Description

In PBHPS, a solar power system and a battery are connected to an output dc bus via a boost converter and a bidirectional buck-boost converter, respectively. Shown in Fig. 1 is a commonly used practical PBHPS, where $v_{of} = v_o H_{of}$ and $v_{\mathrm{batf}} = v_{\mathrm{bat}} H_{bf}$. Here, H_{of} and H_{bf} are the sampling coefficients for the output voltage and the battery voltage, respectively. They are proportionality constants implemented by resistor dividers. Also, K_s is the sampling coefficient for inductor current i_{Lb1} and is also a proportionality constant. The basic control law in the input power distribution aims to provide power to the load primarily by photovoltaic (PV) panels, and when solar power becomes excessive or insufficient, the battery serves as a power storage or backup power source. In practice, MPPT for the PV power system is implemented with the Perturb-and-Observe algorithm [33], which regulates the reference I_{mppt} while the light intensity varies, and forces i_{Lb1} to follow the reference current under the action of the peak current control loop. When the system enters the steady state, I_{mppt} is tracked to the current reference at the maximum power point. The compensation ramp is applied to increase the stability range of peak current controlled converters.

Depending on the amount of available solar power p_{pv} and the state of the battery, the PBHPS has three normal operating modes, as shown in Table I, where P_o is the output power, $V_{b\min}$ and $V_{b\max}$ are the permitted minimum and maximum battery voltages, and $I_{b\max}$ is the charging current limit.

Operating Mode M_1 — If $p_{\mathrm{pv}} < P_o$, the solar power is controlled by the peak current control loop in Fig. 1(b), with the MPPT algorithm enabled, i.e., the peak current reference $I_{\mathrm{ref}} = I_{\mathrm{mppt}}$. The battery provides complementary power through the bidirectional buck-boost converter operating in boost mode to regulate v_o. Thus, in this operating mode, diodes D_c, D_2 and D_3 are off, and D_1 is on.

If p_{pv} is larger than P_o by a small margin, the excessive solar power is used to charge the battery. In this case, the battery charge current is controlled by the energy flow balance, i.e., $p_{\mathrm{pv}} = P_o + p_{\mathrm{bat}}$. Assuming converters are lossless, $p_{\mathrm{bat}} = v_{\mathrm{bat}} i_{\mathrm{bat}}$ is the power absorbed by the battery.

Operating Mode M_2 — If more excessive power is available from the PV panels, causing the charge current i_{bat} to reach the limit $I_{b\max}$, then the bidirectional buck-boost converter operates in buck mode to control charge current, i.e., D_2 is on and D_1 is off . Meanwhile, as excessive power is delivered to the load, v_o increases, causing the error signal v_e to decrease. When it falls below zero, diode D_c is turned on, and v_o is regulated through the voltage loop with an inner peak current control loop, i.e. $I_{\mathrm{ref}} = I_{\mathrm{mppt}} + v_e$. Under this condition, the MPPT algorithm is disabled as v_e is smaller than zero and I_{ref} is regulated by v_e.

Operating Mode M_3 — If $p_{\mathrm{pv}} \geq P_o$ and the battery is fully charged, the constant voltage charging (float charging) loop is enabled to prevent self-discharge of the battery, causing D_3 to turn on and D_2 to turn off.

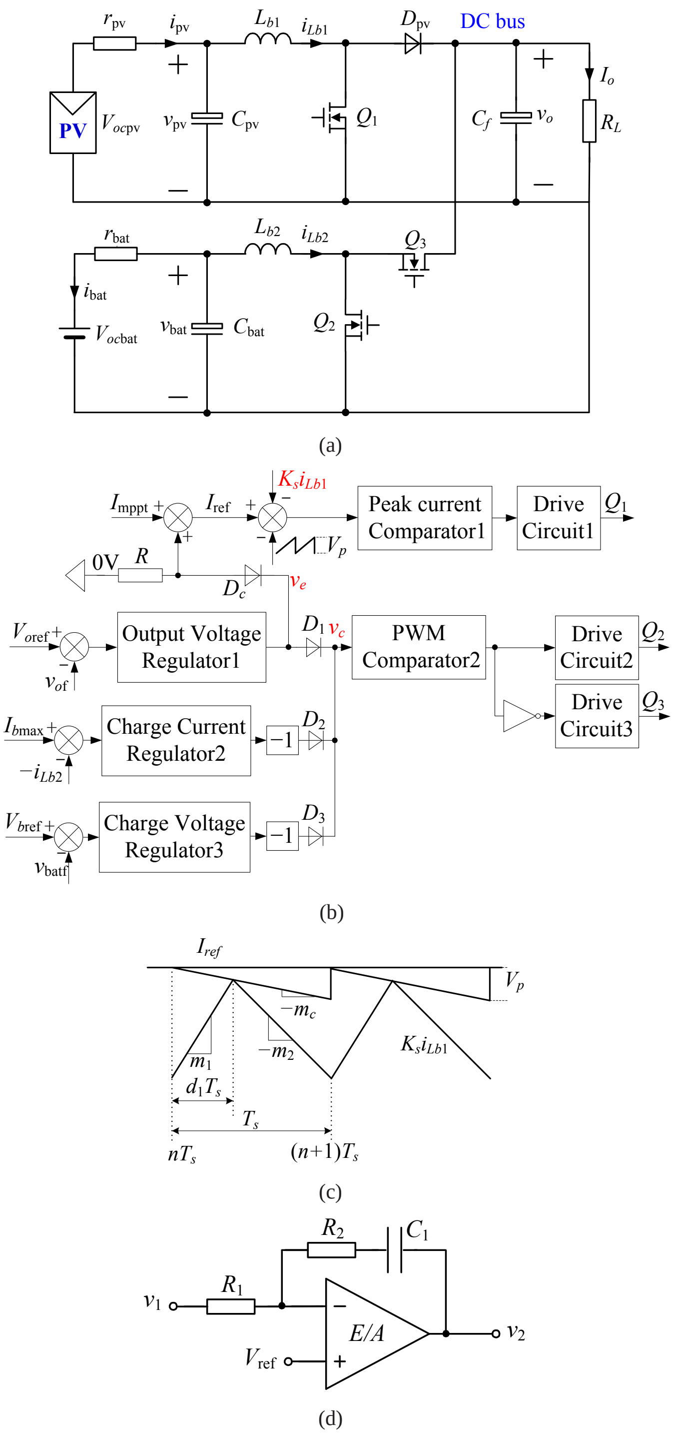

Fig. 1. Photovoltaic-battery hybrid power system. (a) Main topology; (b) control system; (c) typical waveforms for peak current control loop; (d) PI compensator.

TABLE I
Operating Modes and Conditions

	$p_{\mathrm{pv}} < P_o$	$p_{\mathrm{pv}} \geq P_o$ $i_{\mathrm{bat}} < I_{b\max}$	$p_{\mathrm{pv}} \geq P_o$ $i_{\mathrm{bat}} \geq I_{b\max}$
$v_{\mathrm{bat}} \leq V_{b\min}$	shut down	M_1	M_2
$V_{b\min} < v_{\mathrm{bat}} < V_{b\max}$	M_1	M_1	M_2
$v_{\mathrm{bat}} \geq V_{b\max}$	M_1	M_3	M_3

TABLE II
PARAMETERS FOR COMPONENT AND CONTROL SYSTEM USED IN SIMULATION.

T_s	$V_{\rm ocpv}$	$r_{\rm pv}$	I_o	L_{b1}	L_{b2}	$C_{\rm pv}$	C_f	$C_{\rm bat}$	$V_{\rm ocbat}$	$r_{\rm bat}$	V_o	$V_{b\min}$	$V_{b\max}$
10μs	20–34V	50mΩ	0–5A	48μH	48μH	200μF	1880μF	400μF	34–40V	24mΩ	48V	34V	40V
k_{p1}	τ_{f1}	k_{p2}	τ_{f2}	k_{p3}	τ_{f3}	$V_{\rm oref}$	$V_{\rm bref}$	$I_{b\max}$	$I_{\rm mppt}$	$H_{\rm of}$	$H_{\rm bf}$	K_s	V_p
1	0.001–0.6ms	1	0.01ms	10	0.012ms	2.5V	2.5V	3A	0–3A	1/19.2	1/16	0.1	0–0.2V

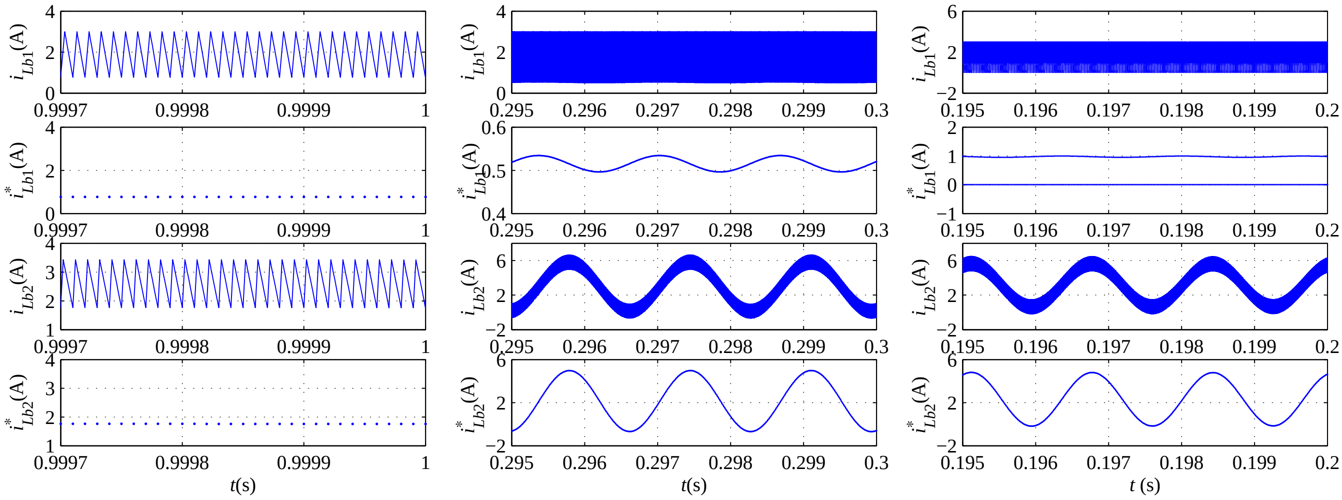

(a) (b) (c)

Fig. 2. Typical simulated waveforms in operating mode M_1 for different values of $V_{\rm ocpv}$, with $V_{\rm ocbat} = 38$ V, $I_{\rm mppt} = 0.3$ A, $\tau_{f1} = 0.475$ ms, $V_p = 0$ V and $I_o = 3.3$ A are kept constant. Upper trace: actual simulated waveforms, lower trace: sampled-data waveform at the beginning of each switching period. (a) Stable period-1 operation with $V_{ocpv} = 32$ V; (b) NS bifurcation with $V_{ocpv} = 26$ V; (c) coexisting fast-scale and slow-scale bifurcation with $V_{ocpv} = 24$ V.

B. Bifurcation Behavior from Simulations

Circuit simulations are performed to examine the stability of PBHPS. In our study, the converter parameters are chosen so that CCM is the default operating mode. The switching frequency of the two converters are the same and trailing edge modulation is used for "PWM Comparator2". First-order proportional-integral (PI) regulators are employed, as shown in Fig. 1(d), and the transfer function is $G_{PI}(s) = k_p\big(1 + 1/(s\tau_f)\big)$, where $k_p = R_2/R_1$ and $\tau_f = R_2C_1$ are the proportional gain and the integral time constant. The parameters used in the simulations are shown in Table II, where V_o is the direct component of v_o; k_{pj} and τ_{fj} $(j = 1, 2, 3)$ are parameters for the jth regulator in Fig. 1(b).

For practical purposes, we examine the dynamic response with $I_{\rm mppt}$, $V_{\rm ocpv}$, R_L, $V_{\rm ocbat}$ and closed-loop parameters serving as the bifurcation parameters, as shown in Figs. 2 and 3. From Fig. 2, the system becomes unstable with slow-scale oscillation when $V_{\rm ocpv}$ is decreased to 26 V. Here the system operates in M_1, and the instability can be recognized as a Neimark-Saker (NS) bifurcation. As $V_{\rm ocpv}$ is further reduced to 24 V, a coexisting fast-scale and slow-scale oscillation will occur [13]. From Fig. 3, we see that the system is stable in the initial operating mode, but it becomes unstable as it switches to another operating mode when the load steps up. Thus, this bifurcation is a non-smooth one. For brevity, we will report the representative smooth and non-smooth bifurcations and will omit the various repetitive details of such bifurcations as they bear no practical consequence to the present study.

III. ANALYSIS BASED ON DISCRETE-TIME MAP

From the foregoing simulation results, we have observed that the system may become unstable through slow-scale bifurcation or fast-scale bifurcation in some particular regions of the parameter space. In this section, we will use a discrete-time model to analyze these bifurcation phenomena. For the purpose of illustration, we consider operating mode M_2, and the same analysis procedure can be applied to other operating modes.

From Fig. 1, the state variable vector of the system can be got as $\boldsymbol{x} = [v_o\ i_{Lb1}\ i_{Lb2}\ v_{\rm pv}\ v_{\rm bat}\ v_e\ v_c]^T$. As CCM operation is assumed, diode $D_{\rm pv}$ and switch Q_3 are always in complementary states to switches Q_1 and Q_2. Then, the state equations for the main circuit are

$$\begin{aligned}
\frac{\mathrm{d}x_1}{\mathrm{d}t} &= \frac{-1}{R_LC_f}x_1 + \frac{1-q_1}{C_f}x_2 + \frac{1-q_2}{C_f}x_3\\
\frac{\mathrm{d}x_2}{\mathrm{d}t} &= \frac{q_1-1}{L_{b1}}x_1 + \frac{1}{L_{b1}}x_4\\
\frac{\mathrm{d}x_3}{\mathrm{d}t} &= \frac{q_2-1}{L_{b2}}x_1 + \frac{1}{L_{b2}}x_5\\
\frac{\mathrm{d}x_4}{\mathrm{d}t} &= \frac{-1}{C_{\rm pv}}x_2 - \frac{1}{r_{\rm pv}C_{\rm pv}}x_4 + \frac{1}{r_{\rm pv}C_{\rm pv}}v_{ocpv}\\
\frac{\mathrm{d}x_5}{\mathrm{d}t} &= \frac{-1}{C_{\rm bat}}x_3 - \frac{1}{r_{\rm bat}C_{\rm bat}}x_5 + \frac{1}{r_{\rm bat}C_{\rm bat}}v_{\rm ocbat}
\end{aligned} \tag{1}$$

where q_1 and q_2 are the switching functions, given as $q_i = 1$ for Q_i is on and $q_i = 0$ for Q_i is off.

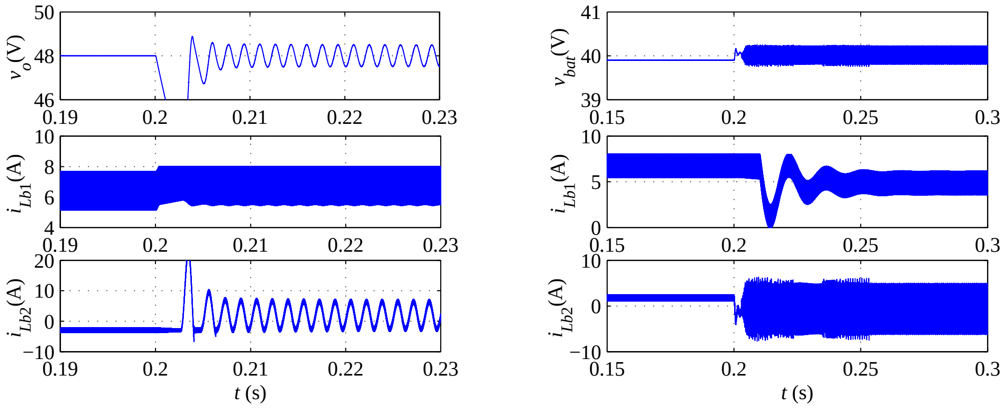

(a) (b)

Fig. 3. Simulated transient waveforms with $V_{\mathrm{ocpv}} = 26$ V and $I_{\mathrm{mppt}} = 0.8$ A. (a) Load current stepped up from 20% load to full load with $V_{\mathrm{ocbat}} = 38$ V and $\tau_{f1} = 0.39$ ms. The system switches from operating mode M_2 to M_1, and slow-scale bifurcation occurs in M_1. (b) Load current stepped down from full load to 20% load with $V_{\mathrm{ocbat}} = 39.99$ V and $\tau_{f1} = 0.6$ ms. The system switches from operating mode M_1 to M_3, and it becomes unstable in M_3.

From the transfer function of PI control and Fig. 1(d), we can write

$$v_2 = k_p\left(1 + \frac{1}{s\tau_f}\right)(V_{\mathrm{ref}} - v_1) \tag{2}$$

Upon differentiating both sides of equation in (2), we get

$$\frac{\mathrm{d}v_2}{\mathrm{d}t} = -k_p\frac{\mathrm{d}v_1}{\mathrm{d}t} - \frac{k_p}{\tau_f}v_1 + \frac{k_p}{\tau_f}V_{\mathrm{ref}} \tag{3}$$

In M_2, the boost converter operates with a dual loop to regulate the bus voltage, whereas the buck-boost converter operates in buck mode to control the charging current, as shown in Fig. 1(b). For the "Output Voltage Regulator1", we substitute $v_1 = v_{of} = H_{of}v_o$ and $v_2 = v_e = x_6$ into (3), and get

$$\frac{\mathrm{d}x_6}{\mathrm{d}t} = -k_{p1}H_{of}\left(\frac{\mathrm{d}x_1}{\mathrm{d}t} + \frac{x_1}{\tau_{f1}}\right) + \frac{k_{p1}}{\tau_{f1}}V_{\mathrm{oref}} \tag{4}$$

For the "Charge Current Regulator2", due to the negative logic, we have $x_7 = v_c = -v_2$, $v_1 = -i_{Lb2}$, and $V_{\mathrm{ref}} = I_{b\mathrm{max}}$. Then, using (3), we have

$$\frac{\mathrm{d}x_7}{\mathrm{d}t} = -k_{p2}\frac{\mathrm{d}x_3}{\mathrm{d}t} - \frac{k_{p2}}{\tau_{f2}}x_3 - \frac{k_{p2}}{\tau_{f2}}I_{b\mathrm{max}} \tag{5}$$

In one switching period, the system toggles among three switch states and the sequence takes the following order: (i): Q_1 and Q_2 are on; (ii): Q_1 is on and Q_2 is off; (iii): Q_1 and Q_2 are both off. Here, as switch Q_2 of the bidirectional buck-boost converter is controlled so that its output voltage is equal to the boost converter's. From Table II and$V_{\mathrm{ocpv}} \le V_{\mathrm{ocbat}}$, we see that the duty cycle of Q_1 is larger than that of Q_2. Accordingly, the switch state "Q_1 is off and Q_2 is on" will not occur. The corresponding state equations for the three switch states can be expressed as

$$\dot{\boldsymbol{x}} = A_{2k}\boldsymbol{x} + B_{2k}\boldsymbol{E}_2 \tag{6}$$

where $k = 1, 2, 3$ is corresponding to the switch state (i), (ii) and (iii), respectively; $\boldsymbol{E}_2$ is the vector of input voltage and reference signals in operating mode M_2, i.e., $\boldsymbol{E}_2 = [V_{\mathrm{ocpv}}\ V_{\mathrm{ocbat}}\ V_{\mathrm{oref}}\ I_{b\mathrm{max}}]^T$. System matrices A_{2k} and B_{2k} are given in (7) which is shown on the top of next page, and (8) below.

$$B_{2k} = \begin{bmatrix} 0 & 0 & 0 & 0 \\ 0 & 0 & 0 & 0 \\ 0 & 0 & 0 & 0 \\ \frac{1}{r_{\mathrm{pv}}C_{\mathrm{pv}}} & 0 & 0 & 0 \\ 0 & \frac{1}{r_{\mathrm{bat}}C_{\mathrm{bat}}} & 0 & 0 \\ 0 & 0 & \frac{k_{p1}}{\tau_{f1}} & 0 \\ 0 & 0 & 0 & -\frac{k_{p1}}{\tau_{f2}} \end{bmatrix} \tag{8}$$

Denote $\boldsymbol{x}_n$ and $\boldsymbol{x}_{n+1}$ as the state variable at the start and the end of the nth switching period, respectively. Using (6), we can derive the solution directly as

$$\begin{aligned} \boldsymbol{x}_{21} &= \boldsymbol{\Phi}_{21}(d_2T_s)\boldsymbol{x}_n + \boldsymbol{\Psi}_{21}(d_2T_s)E_2 \\ \boldsymbol{x}_{22} &= \boldsymbol{\Phi}_{22}\big((d_1-d_2)T_s\big)\boldsymbol{x}_{21} + \boldsymbol{\Psi}_{22}\big((d_1-d_2)T_s\big)E_2 \\ \boldsymbol{x}_{n+1} &= \boldsymbol{\Phi}_{23}\big((1-d_1)T_s\big)\boldsymbol{x}_{22} + \boldsymbol{\Psi}_{23}\big((1-d_1)T_s\big)E_2 \end{aligned} \tag{9}$$

where d_1 and d_2 are the duty cycles of Q_1 and Q_2 in the nth switching period, respectively, which is usually a function of the system's state variables, as will be discussed later; $\boldsymbol{x}_{21}$ and $\boldsymbol{x}_{22}$ are the solution at the end of switch state (i) and (ii); $\boldsymbol{\Phi}_{2k}(\xi)$ and $\boldsymbol{\Psi}_{2k}(\xi)$ $(k = 1, 2, 3)$ are the corresponding transition matrix and system matrix for M_2, given as

$$\begin{aligned} \boldsymbol{\Phi}_{2k}(\xi) &= e^{A_{2k}\xi} = I + \sum_{n=1}^{\infty}\frac{1}{n!}A_{2k}^n\xi^n \\ \boldsymbol{\Psi}_{2k}(\xi) &= \int_0^{\xi}\boldsymbol{\Phi}_{2k}(\xi-\tau)B_{2k}d\tau \end{aligned} \tag{10}$$

By stacking the state variables at the end of each switch state in (9), the discrete-time model can be obtained as

$$\begin{aligned} \boldsymbol{x}_{n+1} = {} & \boldsymbol{\Phi}_{23}\big((1-d_1)T_s\big)\boldsymbol{\Phi}_{22}\big((d_1-d_2)T_s\big)\boldsymbol{\Phi}_{21}(d_2T_s)\boldsymbol{x}_n \\ & +\boldsymbol{\Phi}_{23}\big((1-d_1)T_s\big)\boldsymbol{\Phi}_{22}\big((d_1-d_2)T_s\big)\boldsymbol{\Psi}_{21}(d_2T_s)E_2 \\ & +\boldsymbol{\Phi}_{23}\big((1-d_1)T_s\big)\boldsymbol{\Psi}_{22}\big((d_1-d_2)T_s\big)E_2 \\ & +\boldsymbol{\Psi}_{23}\big((1-d_1)T_s\big)E_2 \\ \stackrel{\mathrm{def}}{=} {} & f(x_n, d_1, d_2, E_2) \end{aligned} \tag{11}$$

$$A_{2k} = \begin{bmatrix} \frac{-1}{R_L C_f} & \frac{1-q_1}{C_f} & \frac{1-q_2}{C_f} & 0 & 0 & 0 & 0 \\ \frac{q_1-1}{L_{b1}} & 0 & 0 & \frac{1}{L_{b1}} & 0 & 0 & 0 \\ \frac{q_2-1}{L_{b2}} & 0 & 0 & 0 & \frac{1}{L_{b2}} & 0 & 0 \\ 0 & \frac{-1}{C_{\mathrm{pv}}} & 0 & \frac{-1}{r_{\mathrm{pv}} C_{\mathrm{pv}}} & 0 & 0 & 0 \\ 0 & 0 & \frac{-1}{C_{\mathrm{bat}}} & 0 & \frac{-1}{r_{\mathrm{bat}} C_{\mathrm{bat}}} & 0 & 0 \\ \frac{k_{p1} H_{of}}{R_L C_f} - \frac{k_{p1} H_{of}}{\tau_{f1}} & \frac{(q_1-1) k_{p1} H_{of}}{C_f} & \frac{(q_2-1) k_{p1} H_{of}}{C_f} & 0 & 0 & 0 & 0 \\ \frac{(1-q_2) k_{p2}}{L_{b2}} & 0 & \frac{-k_{p2}}{\tau_{f2}} & 0 & \frac{-k_{p2}}{L_{b2}} & 0 & 0 \end{bmatrix} \qquad (7)$$

To complete the discrete-time map, the relationship between the duty cycles and the state variables should be derived. During switch states (i) and (ii), Q_1 is always on. Thus, inductor current i_{Lb1} rises, and when the sampled current $K_s i_{Lb1}$ reaches the reference level I_{ref}, switch Q_1 is turned off. Thus, the switching function for Q_1 can be derived as

$$\begin{aligned} s_{21} &= I_{\mathrm{mppt}} + v_e(d_1 T_s) - m_c d_1 T_s - K_s i_{Lb1}(d_1 T_s) \\ &= I_{\mathrm{mppt}} - m_c d_1 T_s + \boldsymbol{C}_1 \boldsymbol{x}_{22} \end{aligned} \qquad (12)$$

where $\boldsymbol{C}_1 = [0 \ -K_s \ 0 \ 0 \ 0 \ 1 \ 0]$, and m_c is the compensation slope given by $m_c = V_p/T_s$.

In the charging current control loop, the "PWM comparator2" compares the error signals v_c with the ramp signal:

$$v_{\mathrm{ramp}} = V_L + m_{\mathrm{ramp}}(t \bmod T_s) \qquad (13)$$

where V_L and m_{ramp} are the lower threshold and rising slope of the ramp signal, respectively. Basically, Q_2 is turned on if $v_c > v_{\mathrm{ramp}}$, and is off otherwise. Then, we can also get a switching function for Q_2, as

$$\begin{aligned} s_{22} &= v_c(d_2 T_s) - v_{\mathrm{ramp}} \\ &= \boldsymbol{C}_2 \boldsymbol{x}_{21} - m_{\mathrm{ramp}} d_2 T_s - V_L \end{aligned} \qquad (14)$$

where $\boldsymbol{C}_2$ is expressed as $\boldsymbol{C}_2 = [0 \ 0 \ 0 \ 0 \ 0 \ 0 \ 1]$.

Combining (11), (12) and (14), an exact discrete-time model is derived. Here, we will investigate the dynamical behavior of the system by examining the movement of the eigenvalues when some chosen parameters are varied. Suppose the equilibrium point is given as $\boldsymbol{x} = \boldsymbol{x}_{e2}$. By setting $\boldsymbol{x}_{n+1} = \boldsymbol{x}_n = \boldsymbol{x}_{e2}$, $s_{21} = 0$ and $s_{22} = 0$, the equilibrium point $\boldsymbol{x}_{e2}$ and steady-state duty cycles D_1 and D_2 can be obtained. Then, the Jacobian, $\boldsymbol{J}_2(\boldsymbol{x}_{e2}) = \partial \boldsymbol{x}_{n+1}/\partial \boldsymbol{x}_n$, evaluated at the equilibrium point can be derived as

$$\boldsymbol{J}_2(\boldsymbol{x}_{e2}) = \frac{\partial f}{\partial \boldsymbol{x}_n} + \frac{\partial f}{\partial d_2}\frac{\partial d_2}{\partial \boldsymbol{x}_n} + \frac{\partial f}{\partial d_1}\frac{\partial d_1}{\partial \boldsymbol{x}_n}\bigg|_{\boldsymbol{x}_n = \boldsymbol{x}_{e2}} \qquad (15)$$

In (15), the relationship between $d_i (i = 1, 2)$ and $\boldsymbol{x}_n$ is implicit in $s_{21} = 0$ and $s_{22} = 0$. Thus, the Jacobian can be derived with implicit function theorem, giving

$$\begin{aligned} \boldsymbol{J}_2(\boldsymbol{x}_{e2}) &= \frac{\partial f}{\partial \boldsymbol{x}_n} - \frac{\partial f}{\partial d_2}\left[\frac{\partial s_{22}}{\partial d_2}\right]^{-1}\frac{\partial s_{22}}{\partial \boldsymbol{x}_n} \qquad (16) \\ &- \frac{\partial f}{\partial d_1}\left[\frac{\partial s_{21}}{\partial d_1}\right]^{-1}\left[\frac{\partial s_{21}}{\partial \boldsymbol{x}_n} + \frac{\partial s_{21}}{\partial d_2}\left[\frac{\partial s_{22}}{\partial d_2}\right]^{-1}\frac{\partial s_{22}}{\partial \boldsymbol{x}_n}\right]_{\boldsymbol{x}_n = \boldsymbol{x}_{e2}} \end{aligned}$$

For brevity, we omit the derivation of the Jacobians for operating modes M_1 and M_3.

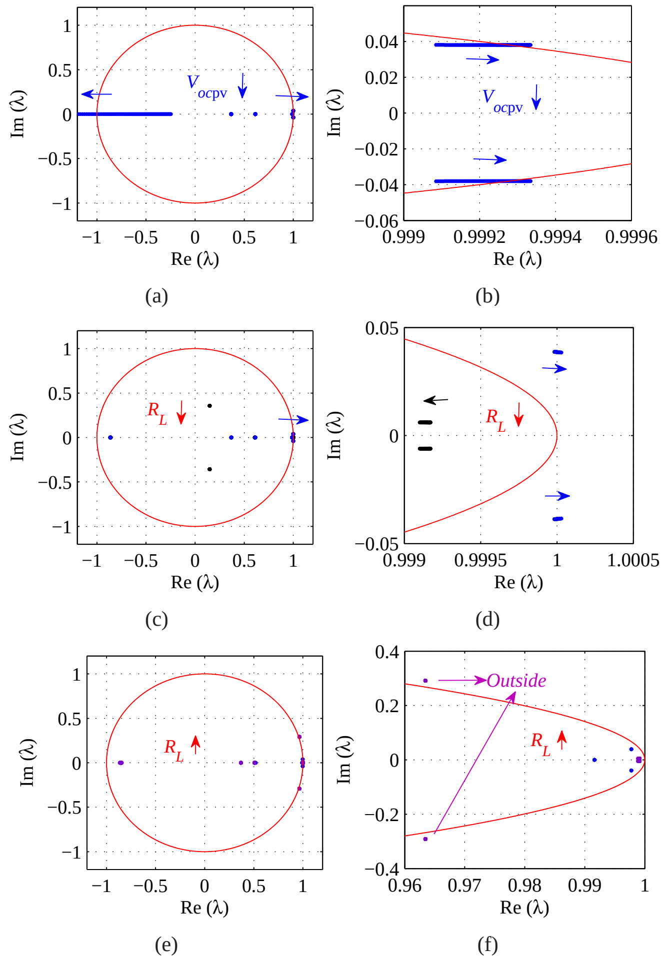

Fig. 4. Loci of eigenvalues for (a) V_{ocpv} is decreased from 34V to 20V with $I_{\mathrm{mppt}} = 0.3$A in M_1; (c) load current increases from 10% load to full load with $I_{\mathrm{mppt}} = 0.8$A and $V_{\mathrm{ocbat}} = 38$V; (e) load current decreases from full load to 10% load with $I_{\mathrm{mppt}} = 0.8$A and $V_{\mathrm{ocbat}} = 39.99$V; (b), (d) and (f) are enlarged views of (a), (c) and (e) showing movement of the pair complex eigenvalues crossing the unit circle. The blue locus corresponds to eigenvalues in M_1, black refers to M_2 and the purple corresponds to M_3. Arrows indicate movement directions of eigenvalues.

Now, we solve the characteristic equation for $\boldsymbol{J}_2(\boldsymbol{x}_{e2})$:

$$\det[\lambda I - \boldsymbol{J}_2(\boldsymbol{x}_{e2})] = 0 \qquad (17)$$

where I is unit matrix. From (17), we can compute all the eigenvalues. If all the eigenvalues are inside the unit circle, the equilibrium state is stable. Any eigenvalue crossing the unit circle from interior to exterior indicates a bifurcation. In particular, if a negative real eigenvalue crosses the unit circle at (–1, 0) point, a fast-scale period-doubling bifurcation

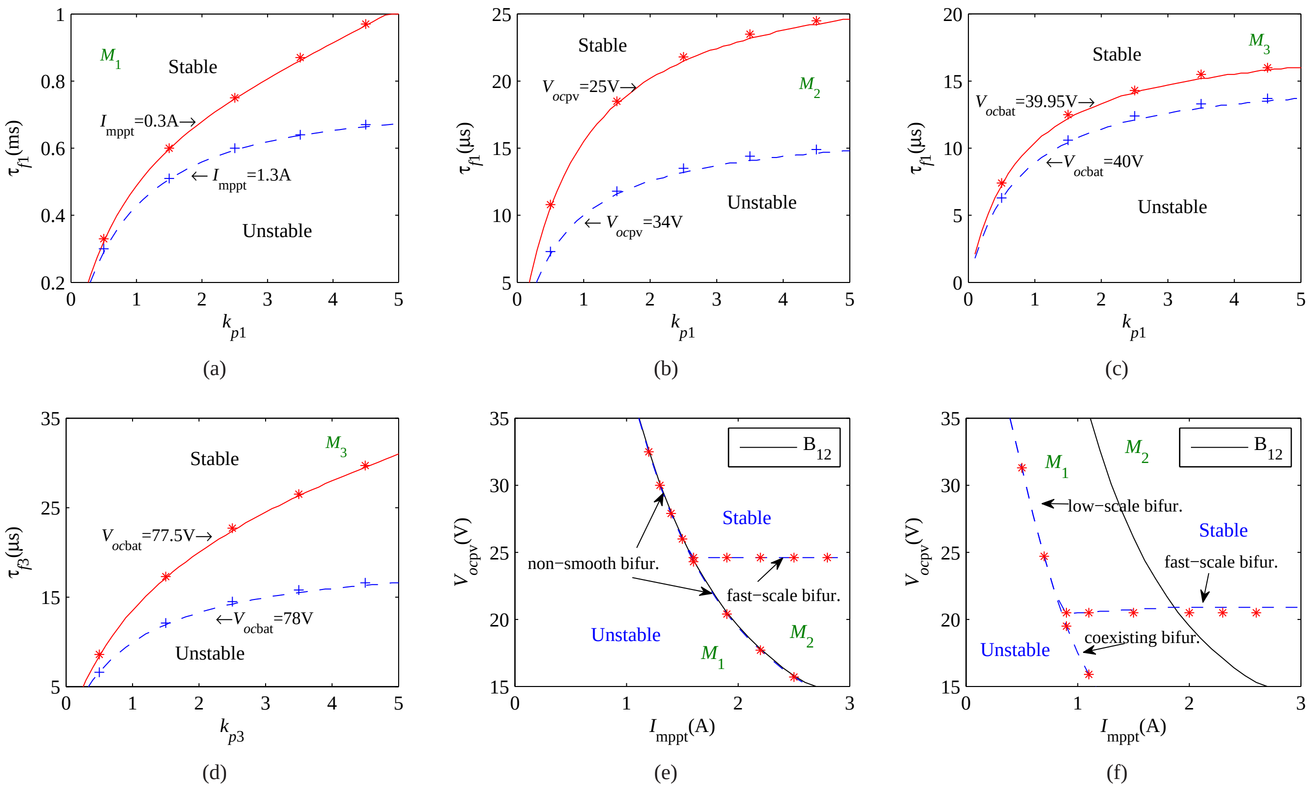

Fig. 5. Stability boundaries in different parameter space. (a)–(d) for different PI parameter space and the bifurcation is slow-scale Neimark-Sacker bifurcation. (a) System operates in M_1, with $V_{ocpv} = 28$ V, $V_{ocbat} = 36$ V, $k_{p3} = 10$, $\tau_{f3} = 0.02$ ms, $I_{\rm mppt} = 2$ A; (b) system operates in M_2, with $V_{ocbat} = 36$ V, $k_{p3} = 10$, $\tau_{f3} = 0.02$ ms, $I_{\rm mppt} = 2$ A; (c)–(d) system operates in M_3 with $V_{ocpv} = 28$ V, $I_{\rm mppt} = 2$ A; (c) $k_{p3} = 10$, $\tau_{f3} = 0.02$ ms; (d) $k_{p1} = 1$, $\tau_{f1} = 0.01$ ms. (e)–(f) for varying sunlight intensity, τ_{f1} and V_p, with $k_{p1} = 1$, $k_{p3} = 10$, $\tau_{f3} = 0.02$ ms and $V_{ocbat} = 36$ V being held constant. (e) $\tau_{f1} = 0.39$ ms, $V_p = 0$ V; (f) $\tau_{f1} = 0.47$ ms, $V_p = 0.08$ V. Points are stability boundaries obtained from circuit simulations. Stable and unstable regions of operation are located above and below the boundary line, respectively.

occurs; and if a pair of complex eigenvalues move out of the unit circle smoothly, the system undergoes a slow-scale NS bifurcation. Here, when both conditions are satisfied, coexistence of the two types of bifurcation is observed [13]. Moreover, if any eigenvalue "jumps" across the unit circle, a non-smooth bifurcation occurs.

Numerical calculations of the eigenvalues are performed. Tables III to V show typical scenarios of the variation of the eigenvalues under the same condition in Figs. 2 and 3. From Table III, we observe the system loses stability via a smooth NS bifurcation as V_{ocpv} is decreased to 26V in M_1. As V_{ocpv} is further decreased, a negative real eigenvalue crosses the (–1, 0) point, and slow-scale and fast-scale oscillations emerge. From Table IV, it can be seen that the number of eigenvalues becomes 6 and the modulus of one complex conjugate pair is larger than unity when the system switches from M_2 to M_1, indicating the occurrence of a non-smooth bifurcation. From Table V, it can be found that the system loses stability as long as the system switches from M_1 to M_3 as the load decreases, then this bifurcation is also a non-smooth one.

The corresponding loci for eigenvalues are plotted in Fig. 4. From Figs. 4(a) and (b), we observe a negative real eigenvalue and a pair of complex eigenvalues which moves through the unit circle smoothly. In Figs. 4(c) and (d), one complex conjugate pair "jumps" off the unit circle when R_L decreases to 39.1 Ω, indicating the occurrence of a non-smooth bifurcation. From Figs. 4(e) and (f), it can be observed that one complex conjugate pair "jumps" off the unit circle as the system switches from M_1 to M_3. These numerical results agree well with the bifurcation phenomena observed in the circuit simulations shown earlier in Figs. 2 and 3.

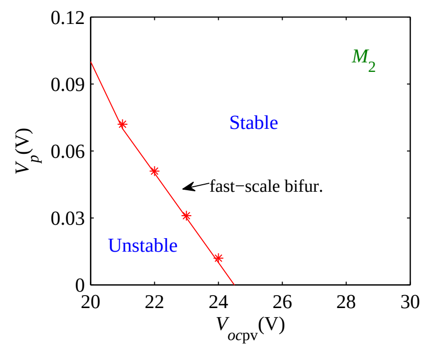

Fig. 6. Stability boundary with V_{ocpv} and V_p serving as bifurcation parameters. Points are stability boundaries obtained from circuit simulations.

IV. Stability Boundaries in Parameter Space

For most practical purposes, only period-1 operation is acceptable, and bifurcation is not permitted. Hence, stability boundaries are very useful design information for engineers

TABLE III
EIGENVALUES FOR DECREASING V_{ocpv} WITH $I_{\text{mppt}} = 0.3\text{A}$ IN OPERATING MODE M_1

V_{ocpv}(V)	Mode	eigenvalues					Modulus	Remarks
32	M_1	-0.49288	0.36751	0.61298	0.98926	$0.99921 \pm j0.03803$	0.99993	Stable
27	M_1	-0.77664	0.36793	0.61298	0.98926	$0.99927 \pm j0.03801$	0.99999	Stable
26	M_1	-0.84601	0.36800	0.61298	0.98926	$0.99928 \pm j0.03800$	1.00000	NS bifurcation
24	M_1	-1.00169	0.36813	0.61298	0.98926	$0.99930 \pm j0.03800$	1.00000	Coexisting

TABLE IV
EIGENVALUES FOR INCREASING LOAD CURRENT (REDUCING LOAD RESISTOR) WITH $I_{\text{mppt}} = 0.8\text{A}$ AND $V_{ocbat} = 38\text{V}$.

$R_L\,(\Omega)$	Mode	eigenvalues					Modulus		Remarks
48	M_2	-0.86349	$0.14803 \pm j0.35684$	$0.99912 \pm j0.00607$	0.36801	0.60789	0.38633	0.99914	Stable
40	M_2	-0.86489	$0.14803 \pm j0.35684$	$0.99910 \pm j0.00606$	0.36801	0.60789	0.38632	0.99912	Stable
39	M_1	-0.86427	$0.99998 \pm j0.03874$	0.36801	0.61298	0.98721		1.00073	slow-scale

TABLE V
EIGENVALUES FOR DECREASING LOAD CURRENT (INCREASING LOAD RESISTOR) WITH $I_{\text{mppt}} = 0.8\text{A}$ AND $V_{ocbat} = 39.99\text{V}$.

$R_L\,(\Omega)$	Mode	eigenvalues					Modulus		Remarks
10	M_1	-0.86413	$0.99776 \pm j0.03916$	0.36799	0.51886	0.99161		0.99853	Stable
13	M_1	-0.86413	$0.99776 \pm j0.03924$	0.36799	0.51886	0.99161		0.99853	Stable
14	M_3	-0.86436	$0.96344 \pm j0.29113$	$0.99886 \pm j0.00478$	0.36798	0.50681	0.99887	1.00647	slow-scale

to identify how far or close the system is from the instability region and in which way the system would loss its stability. In this section, we will generate such stability boundary information. In general, the PI control parameters are important deciding parameters, as k_p need to be set sufficiently large to reduce the steady-state error while τ_f should be small to improve the dynamic response. However, if k_p is too large or τ_f is too small, the system will lose stability. Moreover, in the foregoing sections, we have mentioned that the external parameters, such as V_{ocpv}, I_{mppt}, V_{ocbat} and R_{L} are varying from time to time . It is therefore appropriate to take these parameters as the bifurcation parameters. Corresponding to the choice of component values given in Tables II, Fig. 5 shows the specific stability boundaries obtained through analysis and circuit simulations at full load. From Figs. 5 (a)–(d), the following observations are made:

- The variation of PI parameters will cause slow-scale NS bifurcation. As k_p becomes larger or τ_f becomes smaller, the system loses stability more readily.
- Smooth NS bifurcation can possibly occur in all operating modes under variation of PI parameters, solar intensity, and input voltages.
- Parameters k_{p1} and τ_{f1} affect the system's stability in all operating modes, and they have narrower operating ranges in M_1. Hence, they should be carefully designed in M_1. When the system operates in M_1, the variation of I_{mppt} may alter the stability region, and specifically as I_{mppt} decreases, the stable area shrinks.
- When the system operates in M_2 and M_3, as parameters V_{ocpv} and V_{ocbat} increase, the system will be farther from the instability boundary.

Furthermore, from Figs. 5 (e)–(f), we may draw the following conclusions:

- Smooth slow-scale and fast-scale bifurcations can possibly occur in M_1 and M_2 under variation of I_{mppt}, or V_{ocpv} or even compensation voltage V_p.
- Some parts of the stability boundaries coincide with operating mode boundaries, and they are non-smooth bifurcation boundaries where the system hops from stable to unstable operation as I_{mppt} or V_{ocpv} decreases. For example, referring to (e), when V_{ocpv} is set at 30 V and I_{mppt} at 2 A, the system operates stably in operating mode M_2. If I_{mppt} decreases to 1.3 A, the system will switch from M_2 to M_1 and become unstable, which is a non-smooth bifurcation.
- The input voltage V_{ocpv} not only affects the slow-scale stability boundaries and non-smooth bifurcation, but also has significant effect on fast-scale stability boundaries, and the fast-scale instability area can be effectively reduced with increasing compensation voltage V_p.

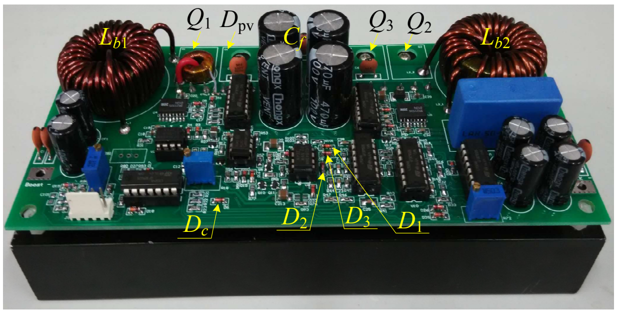

Fig. 7. Experimental prototype of multi-operating-mode PBHPS.

It should be noted that the above procedure generally permits stability boundaries to be generated with any given set of internal and external parameters serving as bifurcation parameters.

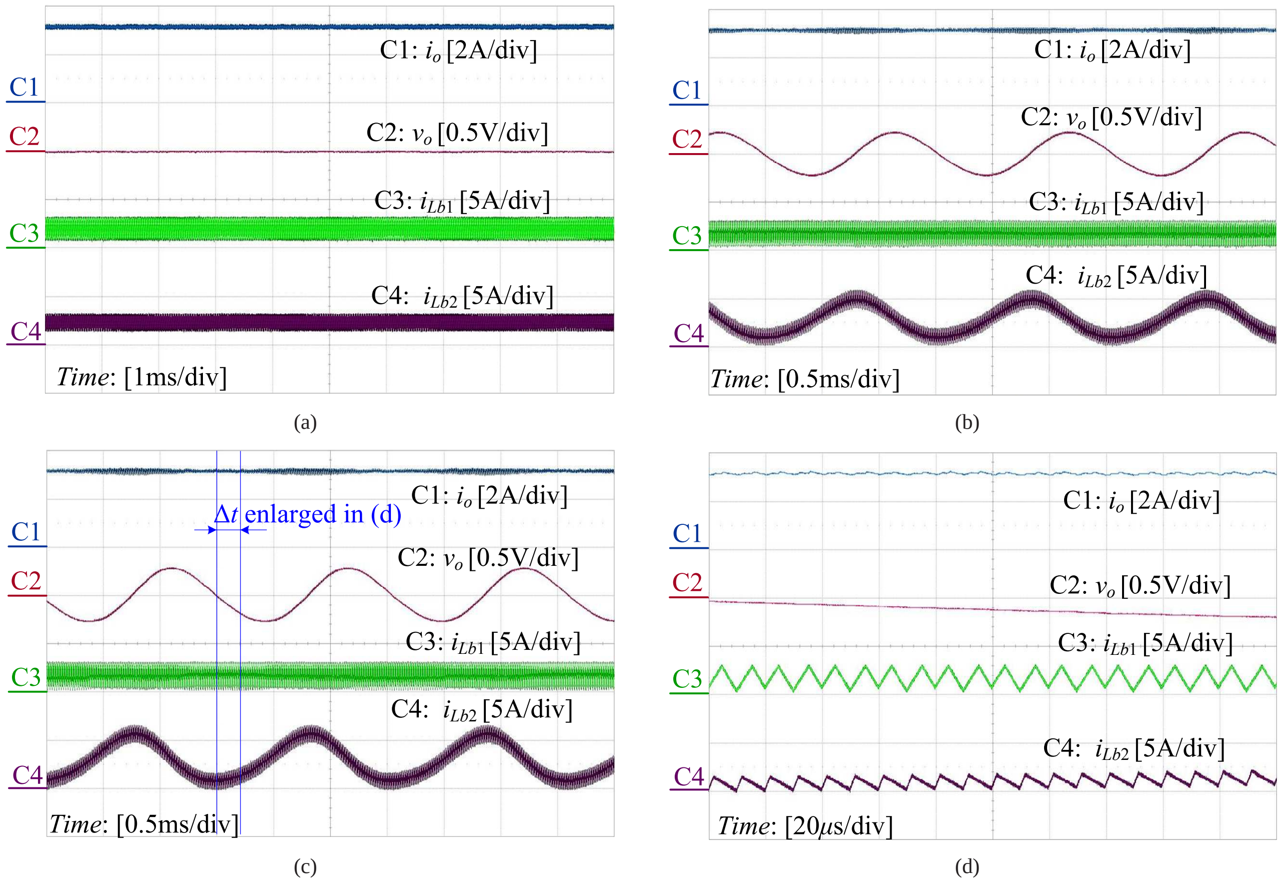

Fig. 8. Typical experimental waveforms in operating mode M_1 for different values of V_{ocpv}, with $V_{ocbat} = 38$ V, $I_{mppt} = 0.3$ A and $I_o = 3.3$ A kept constant. Alternating component of output voltage v_o is shown. (a) Stable period-1 operation with $V_{ocpv} = 32$ V; (b) Neimark-Sacker bifurcation with slow-scale oscillation with $V_{ocpv} = 26$ V; (c) coexisting fast-scale and slow-scale bifurcation with $V_{ocpv} = 24.3$ V; (d) enlarged view of (c).

To avoid bifurcation and ensure the system operates within the desired region, we first find the worst-case operating condition for each control loop from the stability boundaries given in Fig. 5. Then, under the worst-case operating condition, we derive the stability boundaries with control parameters serving as the bifurcation parameters and select appropriate values to ensure stability of the control loop. Thus, the system will be stable under all operating conditions. We take the fast-scale bifurcation as an example here. From Figs. 5 (e)–(f), it can be observed that regardless of the operating mode, fast-scale instability is affected only by V_{ocpv} and V_p, i.e., the peak current control loop loses its stability when V_{ocpv} and V_p are inappropriate. Therefore, to avoid this type of bifurcation, the stability boundary in the (V_{ocpv}, V_p) parameter space can be derived, as shown in Fig. 6. Here we see that the worst-case operating condition for the peak current control loop is when V_{ocpv} assumes the smallest value. Then, the peak current control loop will remain stable under the worst-case operating condition if $V_p > 0.1$. Thus, as long as $V_p > 0.1$, the system exhibits no fast-scale bifurcation under variation of V_{ocpv}.

V. Experimental Verification

A 240 W prototype, as shown in Fig. 7, was built to study the bifurcation phenomena identified and analyzed in the previous sections. The parameters of the prototype used are the same as those used for circuit simulation given in Table II. Fig. 8 shows the experimentally observed slow-scale oscillation and coexisting slow-scale and fast-scale instability in M_1. It can be found that the slow-scale oscillation mainly occurs in the buck-boost converter. This verifies the loss of stability of the output voltage control-loop through a smooth NS bifurcation. A fast-scale oscillation is found in i_{Lb1}, as a result of the peak current control-loop becoming unstable as V_{ocpv} is decreased. These phenomena agree with the simulation results given in Fig. 2 and verify the analysis results in Section III.

A step load change is applied to the PBHPS prototype. Under this test condition, the experimental waveforms are shown in Fig. 9. We can see that the system can properly respond to the step change and switches its operating mode correctly. However, the system becomes unstable while its operating mode is changed, verifying the non-smooth bifurcation as shown earlier in Fig. 3.

The excellent agreement among analysis, circuit simulations and experimental results verifies the ability of the discrete-time mapping model in explaining the smooth bifurcation and non-smooth bifurcation, leading to slow-scale or fast-scale oscillations, as well as coexisting oscillation. The results presented above reveal the salient phenomena. Others are omitted for brevity of presentation.

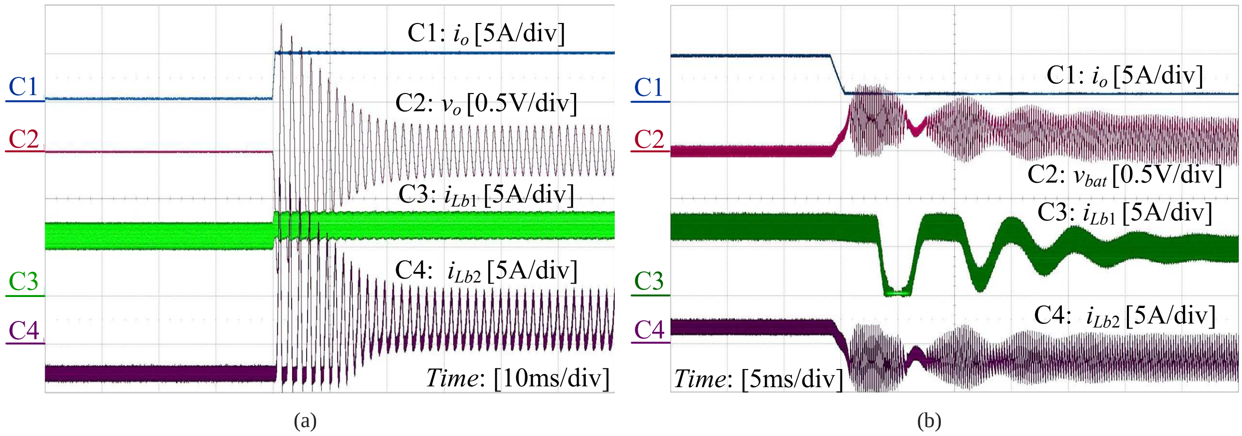

Fig. 9. Transient waveforms with $V_{\rm ocpv} = 26$ V and $I_{\rm mppt} = 0.8$ A. Alternating component of output voltage v_o and battery voltage $v_{\rm bat}$ are shown. (a) Load current steps up from 10% load to full load with $V_{\rm ocbat} = 38$ V and $\tau_{f1} = 0.39$ ms kept constant. The system switches from operating mode M_2 to M_1, and slow-scale bifurcation occurs in M_1. (b) Load current steps down from full load to 20% load with $V_{\rm ocbat} = 39.99$ V and $\tau_{f1} = 0.6$ ms kept constant. The system switches from operating mode M_1 to M_3, and slow-scale bifurcation occurs in M_3.

VI. Conclusions

Due to the intermittent nature of the availability of renewable energy, hybrid renewable power generation systems are usually designed to operate with multiple structures and multiple operating modes. The dynamical behavior of such systems is thus rather complex and the design for stable period-1 operation is non-trivial. A commonly used multi-operating-mode stand-alone is studied in detail in this paper to illustrate the complex behavior of this kind system. The photovoltaic-battery hybrid power system is found to lose stability via a smooth Neimark-Sacker bifurcation, period-doubling bifurcation, or a non-smooth bifurcation. These phenomena have been thoroughly analyzed with a discrete-time model. Moreover, stability boundaries are derived in a design-oriented form, allowing critical operation conditions be readily extracted for identification of stable operating regions. Salient bifurcation phenomena were demonstrated in an experimental prototype. The smooth and non-smooth bifurcation observed in this paper are generic to the multi-structure and multi-operating mode power system, and this line of research is highly relevant to the design of renewable energy systems that have inherent multiple structures and mandatorily operate with multiple modes.

References

[1] M. H. Nehrir, C. Wang, K. Strunz, H. Aki, R. Ramakumar, J. Bing, Z. Miao, and Z. Salameh, “A review of hybrid renewable/alternative energy systems for electric power generation: configurations, control, and applications,” *IEEE Trans. Sustain. Energy,* vol. 2, no. 4, pp. 392–403, Oct. 2011.

[2] Z. Qian, O. Abdel-Rahmam, and I. Batarseh, “An integrated four-port dc/dc converter for renewable energy applications,” *IEEE Trans. Power Electron.*, vol. 25, no. 7, pp. 1877–1887, July 2010.

[3] J. Imhoff, J. R. Pinheiro, J. L. Russi, D. Brum, R. Gules, and H. L. Hey, “DC-DC converters in a multi-string configuration for stand-alone photovoltaic system,” in *IEEE Power Electron. Specialists Conf. Record,* 2008, pp. 2806–2812.

[4] D. Xu, L. Kang, L. Chang, and B. Cao, “Optimal sizing of standalone hybrid wind/PV power systems using genetic algorithms,” in *Proc. IEEE Canadian Conf. Elect. Comp. Eng.,* 2005, pp. 1722–1725.

[5] K. Agbossou, M. Kolhe, J. Hamelin, and T. K. Bose, “Performance of a stand-alone renewable energy system based on energy storage as hydrogen,” *IEEE Trans. Energy Conv.*, vol. 19, no. 3, pp. 633–640, Sept. 2004.

[6] J. Schönberger, R. Duck, and S. D. Round, “DC-Bus signaling: a distributed control strategy for a hybrid renewable nanogrid,” *IEEE Trans. Ind. Electron.*, vol. 53, no. 5, pp. 1453–1460, Oct. 2006.

[7] Z. Jiang, “Power management of hybrid photovoltaic-fuel cell power systems,” in *Proc. IEEE Power Eng. Society General Meeting*, 2006, 1-4244-0493-2.

[8] J. Zhang and L. Ji, “An effective hybrid energy storage system based on battery-EDLC for distributed generation systems,” in *Proc. IEEE Conf. Ind. Electron. Appl.*, 2010, pp. 819–824.

[9] J. Xiao and P. Wang,“Multiple modes control of household DC microgrid with integration of various renewable energy sources,” in *IEEE Ind. Electron. Conf. Record*, 2013, pp. 1773–1778.

[10] Y. Gu, X. Xiang, W. Li, and X. He, “Mode-adaptive decentralized control for renewable DC microgrid with enhanced reliability and flexibility,” *IEEE Trans. Power Electron.*, vol. 29, no. 9, pp. 5072–5080, Sept. 2014.

[11] H. Matsuo, W. Lin F. Kurokawa, T. Shigemizu, and N. Watanabe, “Characteristics of the multiple-input dc-dc converter,” *IEEE Trans. Ind. Electron.*, vol. 51, no. 3, pp. 625–631, June 2004.

[12] C. Zhao, S. D. Round, and J. W. Kolar, “An isolated three-port bidirectional DC-DC converter with decoupled power flow management,” *IEEE Trans. Power Electron.*, vol. 23, no. 5, pp. 2443–2453, Sept. 2008.

[13] Y. Chen, C. K. Tse, S. Qiu, L. Lindenmüller, and W. Schwarz, “Coexisting fast-scale and slow-scale instability in current-mode controlled dc/dc converters: analysis, simulation and experimental results,” *IEEE Trans. Circ. Syst. I—Reg. Papers*, vol. 55, no. 10, pp. 3335–3348, Nov. 2008. 1992.

[14] C. K. Tse, “Flip bifurcation and chaos in three-state switching boost regulators,” *IEEE Trans. Circ. Syst. I: Fundam. Theory Appl.*, vol. 41, no. 1, pp. 16-23, Jan. 1994.

[15] C. K. Tse, “Chaos from a buck switching regulator operating in discontinuous mode,” *Int. J. Circ. Theory Appl.*, vol. 22, no. 4, pp. 263–278, Jul-Aug. 1994.

[16] W. C. Y. Chan and C. K. Tse, “Study of bifurcations in current-programmed dc/dc boost converters: from quasi-periodicity to period-doubling,” *IEEE Trans. Circ. Syst. I—Fundam. Theory Appl.*, vol. 44, no. 12, pp. 1129–1142, Oct. 1997.

[17] C. K. Tse, *Complex Behavior of Switching Power Converters,* Boca Raton: CRC Press, 2003.

[18] D. C. Hamill, J. H. B. Deane, and D. J. Jefferies, “Modeling of chaotic dc-dc converters by iterated nonlinear mappings,” *IEEE Trans. Power Electron.*, vol. 7, no. 1, pp. 25–36, Jan. 1992.

[19] A. El Aroudi, L. Benadero, E. Toribio, and G. Olivar, “Hopf bifurcation and chaos from torus breakdown in a pwm voltage-controlled dc-dc boost converter,” *IEEE Trans. Circ. Syst. I: Fundam. Theory Appl.*, vol. 46, no. 11, pp. 1374–1382, Nov. 1999.

[20] Y. Ma, C. K. Tse, T. Kousaka, and H. Kawakami, “Connecting border collision with saddle-node bifurcation in switched dynamical systems,”

IEEE Trans. Circ. Syst. II: Express Briefs, vol. 52, no. 9, pp. 581–585, 2005.

[21] C. K. Tse and M. di Bernardo, "Complex behavior in switching power converters," *IEEE Proceedings*, vol. 90, no. 5, pp. 768–781, 2002.

[22] S. Banerjee, P. Ranjan, and C. Grebogi,"Bifurcations in two-dimensional piecewise smooth maps-theory and applications in switching circuits," *IEEE Trans. Circ. Syst. I: Fundam. Theory Appl.*, vol. 47, no. 5, pp. 633–643, May 2000.

[23] C. K. Tse, Y. M. Lai, and H. H. C. Iu, "Hopf bifurcation and chaos in a free-running current-controlled Ćuk switching regulator," *IEEE Trans. Circ. Syst. I: Fundam. Theory Appl.*, vol. 47, no. 4, pp. 448–457, Apr. 2000.

[24] S. C. Wong, X. Wu, and C. K. Tse, "Sustained slow-scale oscillation in higher order current-mode controlled converter," *IEEE Trans. Circ. Syst. II: Express Briefs*, vol. 55, no. 5, pp. 489–493, May 2008.

[25] V. Moreno-Font, A. El Aroudi, J. Calvente, R. Giral, and L. Benadero, "Dynamics and stability issues of a single-inductor dual-swithing dc-dc converter," *IEEE Trans. Circ. Syst. I: Reg. Papers*, vol. 57, no. 2, pp. 415–426, Feb. 2010.

[26] H. H. C. Iu and C. K. Tse, "Bifurcation behavior of parallel-connected buck converters," *IEEE Trans. Circ. Syst. I: Fundam. Theory Appl.*, vol. 48, no. 2, pp. 233–240, Feb. 2001.

[27] H. H. C. Iu and C. K. Tse, "Study of low-frequency bifurcation phenomena of a parallel-connected boost converter system via simple averaged models," *IEEE Trans. Circ. Syst. I: Fundam. Theory Appl.*, vol. 50, no. 5, pp. 679–686, May 2003.

[28] M. Huang, S. C. Wong, C. K. Tse, and X. Ruan, "Catastrophic bifurcation in three-phase voltage-source converters," *IEEE Trans. Circ. Syst. I: Reg. Papers*, vol. 60, no. 4, pp. 1062–1071, Apr. 2013.

[29] M. Huang, C. K. Tse, S. C. Wong, C. Wan, and X. Ruan, "Low-frequency Hopf bifurcation and its effects on stability margin in three-phase PFC power supplies connected to non-ideal power grid," *IEEE Trans. Circ. Syst. I: Reg. Papers*, vol. 60, no. 12, pp. 3328–3340, Dec. 2013.

[30] C. Wan, M. Huang, C. K. Tse, S. C. Wong, and X. Ruan, "Nonlinear behavior and instability in three-phase boost rectifier connected to non-ideal power grid with interacting load," *IEEE Trans. Power Electron.*, vol. 28, no. 7, pp. 3255–3265, Jul. 2013.

[31] X. Xiong, C. K. Tse, and X. Ruan, "Smooth and non-smooth bifurcations in multi-structure multi-operating-mode hybrid power systems," *Int. J. Bifurcation and Chaos*, vol. 23, no. 5, pp. 1–12, May 2013.

[32] X. Xiong, C. K. Tse, and X. Ruan, "Bifurcation analysis of standalone photovoltaic-battery hybrid power system," *IEEE Trans. Circ. Syst. I: Reg. Papers*, vol. 60, no. 5, pp. 1354–1365, May 2013.

[33] T. Esram and P. L Chapman, "Comparison of photovoltaic array maximum power point tracking techniques," *IEEE Trans. Energy Conv.*, vol. 22, no. 2, pp. 439–449, June, 2007.

Xiaoling Xiong (S'11) received the BEng and MEng degrees from Nanjing University of Aeronautics and Astronautics, Nanjing, China, in 2007 and 2010, respectively. She is currently working toward the PhD degree at Nanjing University of Aeronautics and Astronautics, Nanjing, China.

She spent a short time with the Lighting Department of GE (China) Research and Development Center Co. Ltd., as an intern in 2010, and worked as a Research Assistant in the Department of Electronic and Information Engineering at Hong Kong Polytechnic University, from February 2011 to July 2012. Her main research interests include modeling, analysis and design power electronic systems and study the complex behavior in power electronic circuits.

Chi K. Tse (M'90–SM'97–F'06) received the BEng (Hons) degree with first class honors in electrical engineering and the PhD degree from the University of Melbourne, Australia, in 1987 and 1991, respectively. He is presently Chair Professor of Electronic Engineering at the Hong Kong Polytechnic University, Hong Kong. From 2005 to 2012, he was the Head of Department of Electronic and Information Engineering at the same university. His research interests include complex network applications, power electronics and chaos-based communications.

Currently Dr. Tse serves as Editor-in-Chief for the *IEEE Circuits and Systems Magazine* and Editor-in-Chief of *IEEE Circuits and Systems Society Newsletter*. He was/is an Associate Editor for the IEEE Transactions on Circuits And Systems Part I—Fundamental Theory and Applications from 1999 to 2001 and again from 2007 to 2009. He has been an Associate Editor for the IEEE Transactions on Power Electronics and IEEE Journal of Emerging and Selected Topics on Power Electronics since 1999 and 2013, respectively. He is an Editor of the *International Journal of Circuit Theory and Applications* and is an Honorary Member of the Editorial Board of the *International Journal and Bifurcation and Chaos*.

Dr. Tse received the L.R. East Prize from the Institution of Engineers, Australia, in 1987, the Best Paper Award from IEEE Transactions on Power Electronics in 2001 and the Best Paper Award from *International Journal of Circuit Theory and Applications* in 2003. In 2005 and 2011, he was selected and appointed as IEEE Distinguished Lecturer. In 2007, he was awarded the Distinguished International Research Fellowship by the University of Calgary, Canada. In 2009 and 2013, he and his co-inventors won the Gold Medal at the International Exhibition of Inventions of Geneva, Switzerland, on LED lighting technologies. In 2011, he was appointed Honorary Professor by RMIT University, Melbourne, Australia. He was awarded the Gledden Fellowship and the Distinguished International Fellowship, in 2013 and 2015, respectively, by the University of Western Australia, Perth, Australia.

Xinbo Ruan (M'97–SM'02) was born in Hubei Province, China, in 1970. He received the BS and PhD degrees in electrical engineering from Nanjing University of Aeronautics and Astronautics (NUAA), Nanjing, China, in 1991 and 1996, respectively.

In 1996, he joined the Faculty of Electrical Engineering Teaching and Research Division, NUAA, where he became a Professor in the College of Automation Engineering in 2002 and has been engaged in teaching and research in the field of power electronics. From August to October 2007, he was a Research Fellow in the Department of Electronic and Information Engineering, Hong Kong Polytechnic University, Hong Kong, China. Since March 2008, he has been also with the College of Electrical and Electronic Engineering, Huazhong University of Science and Technology, China. He is a Guest Professor with Beijing Jiaotong University, Beijing, China, Hefei University of Technology, Hefei, China, and Wuhan University, Wuhan, China. He is the author or co-author of four books and more than 100 technical papers published in journals and conferences. His main research interests include soft-switching dc-dc converters, soft-switching inverters, power factor correction converters, modeling the converters, power electronics system integration and renewable energy generation system.

Dr. Ruan was a recipient of the Delta Scholarship by the Delta Environment and Education Fund in 2003 and was a recipient of the Special Appointed Professor of the Chang Jiang Scholars Program by the Ministry of Education, China, in 2007. Since 2005, he has been serving as Vice President of the China Power Supply Society, and since 2008, he has been a member of the Technical Committee on Renewable Energy Systems within the IEEE Industrial Electronics Society. He has been an Associate Editor for the IEEE Transactions on Industrial Electronics and the IEEE Journal of Emerging and Selected Topics on Power Electronics since 2011 and 2013, respectively. He is a Senior Member of the IEEE Power Electronics Society and the IEEE Industrial Electronics Society.